Additive Manufacturing 60 (2022) 103236

Contents lists available at ScienceDirect

Additive Manufacturing

journal homepage: www.elsevier.com/locate/addma

Differences in micro grain/fiber distributions between matrix and interlayer of cementitious filaments affected by extrusion molding

Rijiao Yang [a,b], Yi Zhu [a,c,d], Yan Lan [a], Qiang Zeng [a,*], Yu Peng [a], Zhendi Wang [b,e,**]

[a] College of Civil Engineering and Architecture, Zhejiang University, Hangzhou 310058, China
[b] State Key Laboratory of Green Building Materials, China Building Materials Academy, Beijing 100024, China
[c] Center for Balance Architecture, Zhejiang University, Hangzhou 310058, China
[d] The Architectural Design & Research Institute of Zhejiang University Co., Ltd., Hangzhou, 310028, China
[e] School of Materials Science and Engineering, Chang'an University, Xi'an 710061, China

ARTICLE INFO

Keywords:
Extrusion
Glass fibers
Directional orientation
Interface

ABSTRACT

Extrusion molding generally causes laminar structure with obvious interfaces, however, the impacts of extrusion molding on the distributions of micro grains/fibers in the matrix and interface of filaments haven't been fully addressed. Herein, X-ray computed tomography was employed to track the cement micro particles and glass microfibers in extrusion molded cementitious composites (EMCC). Results show that small grains migrated into the interface while coarse grains stayed in the matrix of filaments. Glass microfibers in the matrix and interface were roughly parallel and perpendicular to the printing direction, respectively. The mechanisms of shearing stress gradients built in the EMCC filaments and collisions on the microfibers during pumping were proposed to account for the featured distributions and directions of the micro grains and fibers. The findings would deepen the understandings in particle redistribution in non-Newtonian liquid during extrusion molding and facilitate the design and development of 3D printing construction materials.

1. Introduction

Three-dimensional (3D) printing is a widely used automatic construction technique that builds a structure through the pattern of material addition [1,2] and shows great benefits in structure design, manpower saving, and clean construction environments [3,4]. For the scenarios of 3D printing constructions, extrusion molding is probably the most widely used technique due to its high printing efficiency, simple printing equipment and low cost [5,6]. With the unique printing pattern, extrusion molding significantly affects phases (fiber and particle) distribution during pumping. This issue has not been fully addressed especially when micro grains and microfibers with high slenderness and low stiffness are involved.

During extrusion printing, the materials, asking for a delicate balance among viscosity, flowability and thixotropy [7–9], are pumped through a pipe and then extruded though a nozzle to form uniform and controllable filaments, whose yield strength should rapidly grow to resist itself and upper gravity [10,11]. The need of material properties and formless construction strictly limit the migration of phases in cementitious composite after printing [12–14]. This is quite different from conventional cementitious materials casting, where sufficient vibrations or stirrings may cause obvious particle redistribution, so isotropic microstructures and engineering properties can be built [15,16]. For extrusion molding, however, cementitious materials are subjected to non-uniform shearing actions during the pumping process [17,18]. Specifically, less shearing forces are exerted to the core filament (plug flowing) with lower shearing rate and faster flowing speed, while larger shearing forces are exerted on the edge of the filament with higher shearing rate [19,20]. The viscosity of cementitious slurries decreases non-linearly with the increase of shearing rate, following a viscosity-shearing rate regime of non-Newtonian fluid [21,22]. The gradients of shear stress and viscosity built in the printing tube can cause the special and uneven distribution of particles after the slurries are extruded [23]. A transparent model concrete flowing test implied that, in the process of pumping, large particles move towards the core area and small particles are more likely to gather in the edge of the printing tube [24]. Similar findings were documented elsewhere [17,19]. However, when regarding to the distribution of cement grains, a main phase

* Corresponding author.
** Corresponding author at: State Key Laboratory of Green Building Materials, China Building Materials Academy, Beijing 100024, China.
E-mail addresses: cengq14@zju.edu.cn (Q. Zeng), wzhendi@163.com (Z. Wang).

https://doi.org/10.1016/j.addma.2022.103236
Received 7 August 2022; Received in revised form 19 September 2022; Accepted 15 October 2022
Available online 19 October 2022
2214-8604/

Table 1
Physical properties and chemical composition of the cement.

Fineness (0.08 mm sieve /%)	Density (g/cm^3)	Specific surface (m^2/kg)	Standard consistency (%)	Soundness (mm)	Setting time (min)		Flexural strength (MPa)		Compressive strength (MPa)	
					Initial	Final	3 d	28 d	3 d	28 d
0.8	3.15	338	25.2	0.5	138	215	6.4	9.0	29.7	51.0
Chemical composition	SiO_2	Al_2O_3	Fe_2O_3	CaO	MgO	SO_3	Na_2Oeq	f-CaO	Loss	Cl-
Content/%	21.8	4.55	3.45	64.4	2.9	2.45	0.532	0.93	1.27	0.011

that acts as the binding material in extrusion molding cementitious composites (EMCC), the relevant research, to the best knowledge of the authors, has not been reported.

Another interesting but unaddressed issue for particle distribution in EMCC is the distribution and direction of particles with high slenderness. The highly slender particles in EMCC can be specified as fibers. Fibers in different types (e.g., carbon fiber, steel fiber, glass fiber, polymer fiber, mineral fibers) and sizes (from microns to millimeters in diameter) are often used to reinforce EMCC [25–31]. For example, wollatonite microfibers were employed to fabricate EMCC with good printing performances and mechanical strengths [30,31]. The reinforcement is greatly affected by both the spatial and directional distributions of the fibers used in EMCC. Previous studies indicated that steel fibers are difficult to stay in the interlayer zone between filaments [27, 32]. A number of studies have shown that aligned fibers help to improve compressive, flexural and tensile properties compared with randomly distributed fibers [33–35]. Fiber orientation could be influenced by extrusion parameters [15,36], flow patterns, wall effect of formworks and external electromagnetic field for steel fibers [26]. The properties of materials and printing parameters, such as viscosity [37] and yield strength [38] can also impact fiber orientation. It was demonstrated that the non-uniform shearing effect during the pumping extrusion process again contributes to the alignment of macro fibers along the printing direction [28,39,40]. Pham et al. [27] detected the directional and spatial distribution of steel fibers in EMCC by X-ray micro-computed tomography (XCT) and testified the strongly orientated distribution of the fibers in the EMCC matrix. Arunothayan et al. [15] evaluated the fiber alignment in an EMCC reinforced with steel fibers by the 2D image processing technique. It is noteworthy that steel fibers generally possess high modulus or stiffness, so the gradients of shearing forces during the extrusion process would have minor effect on the fibers themselves. For these fibers with low stiffness and high slenderness, the non-uniform shearing forces may torture the fibers in the printing process. So non-uniform fiber orientation and distribution may occur for EMCC with soft fibers. For example, 3D printed polymer composites with glass microfibers that have large slenderness (L/D= 461.5) showed that the fibers were disorderly distributed in the core area and the edge area of the pipeline, and showed strongly orientated distribution only in the non-uniform shearing area [41,42]. It is therefore greatly curious what are the orientation and spatial distribution of glass microfibers in EMCC after extrusion molding.

To address the above questions, in this work, EMCCs with two dosages of glass microfibers (0.3% and 0.6%) were fabricated and the spatial distribution and direction of the cement grains and glass microfibers were resolved by XCT. Elaborate analyses on the size and orientation distributions of cement grains and glass microfibers were performed. A layer-by-layer imaging analysis was specifically used to quantify the differences in particles' distributions and fibers' orientation between the filaments' matrix and interface. The mechanisms of extrusion molding effected particle redistribution in EMCC were profoundly discussed.

Table 2
Mix proportions of the 3D-printed EMCC.

Sample ID	Water /wt%	Cement /wt%	Accelerator /wt%	HPMC /wt%	PCE-SP /wt %	Glass fiber /wt%
EMCC-3	30	100	2.25	0.15	0.44	0.3
EMCC-6	30	100	2.25	0.15	0.44	0.6

2. Materials and methods

2.1. Raw materials

A Portland cement (Type PI 42.5 according to a Chinese standard) was used as the only binder for EMCC fabrication. No other inorganic fillers were added so that the anhydrous cement grains can be tracked after extrusion molding. For the mix proportions of EMCC, water-to-cement (w/c) ratio of 0.3, Hydroxypropyl methylcellulose (HPMC, from Renqiu Shuangcheng Chemical Products Factory, Shangdong, China) of 0.15 wt% (in reference to cement weight), polycarboxylate superplasticizer (PCE-SP, from Huawei Yinkai Building Materials Technology, Shangdong, China) of 0.44 wt%, and alkali accelerator (from Jiaozuo Xinzhuwang Material Technology Company, Henan, China) of 2.25 wt% were used. The compositions and physical properties of the cement are listed in Table 1.

Glass microfibers with 14 μm in diameter (D) and 6 mm in length (L) (L/D = 429) were used to reinforce the cementitious materials (see Appendix A). Two glass microfibers contents of 0.3 wt% and 0.6 wt% were used. The relevant low fiber contents were designed to avoid the possible agglomerations of glass microfibers that would obstruct the printing nozzle [16,28]. Details of the mix proportions are listed in Table 2.

2.2. Sample preparation

Fresh EMCC slurries were prepared according to the mix proportions shown in Table 2. First, the solids including cement, alkali accelerator and HPMC experienced a dry-mixing in a mixing bowl with low-speed stirrings of 60 r/min for 30 s. Later, a PCE-SP water solution was prepared by mixing the PCE-SP powder in water with sufficient hand stirrings, and was poured into the mixing bowl followed by high-speed stirrings of 120 r/min for 120 s. Subsequently, glass microfibers were mixed with the neat cement slurries with the high-speed stirrings of 120 r/min for 60 s to generate the slurries of glass microfiber reinforced cementitious slurries. In this work, the glass microfibers were artificially dispersed and gradually added into the cement slurries, and manual agitations were employed to randomize the distribution of the glass microfibers. After that, the flowability and viscosity of the prepared cementitious slurries were tested. The flowability of EMCC slurries was tested as follows: the slurries were poured into the truncated cone (with the upper diameter of 36 mm, lower diameter of 60 mm and height of 60 mm); then the cone was removed, the expansion of the slurries was measured after 30 s. The slump flows of EMCC3 and EMCC6 were 93.4 mm and 91.7 mm, respectively. Viskomat XL (Germany) was used to test viscosity of the EMCCs. The maximum speed of 120 rpm was obtained in 4 min and the speed slowed down to zero in next 4 min. Results showed

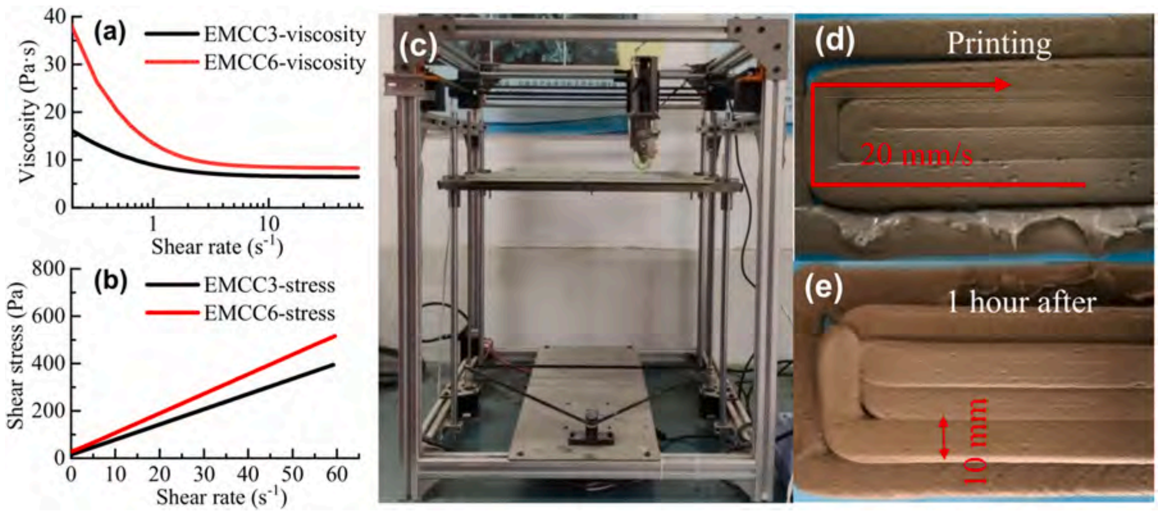

Fig. 1. Viscosity (a) and stress (b) of EMCC3 and EMCC6 slurries tested at different shear rates; (c) image of 3D cementitious composites printer; (d) in-situ extrusion molding with the printing speed of 20 mm/s, and (e) the hardened EMCC structure (after 1 h).

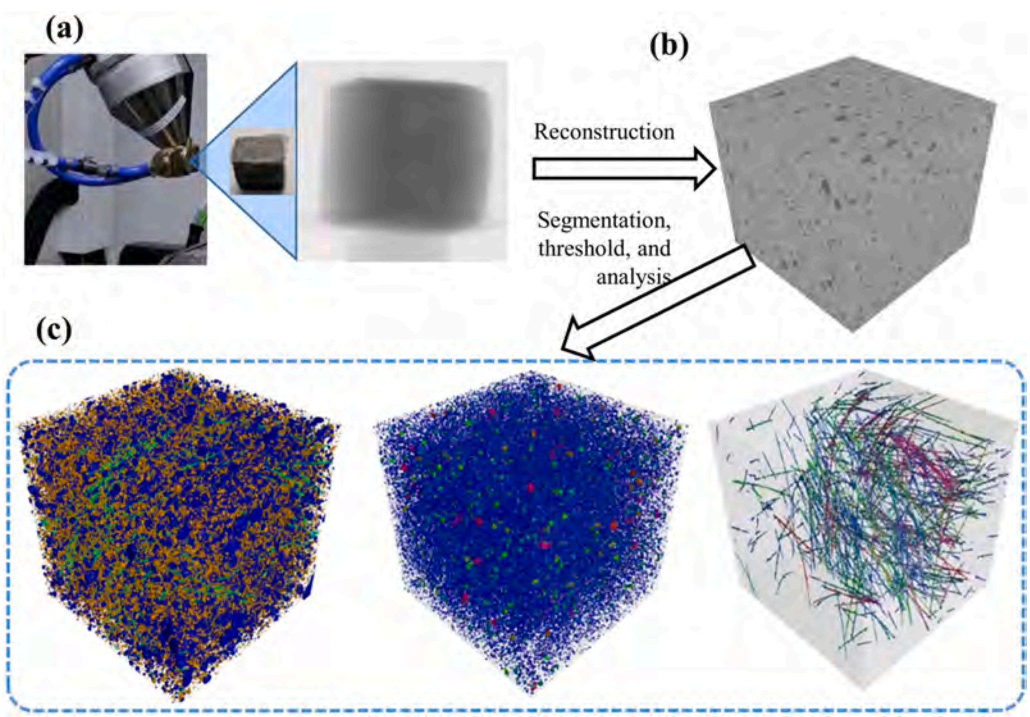

Fig. 2. Test and data processing by micro-XCT: (a) XCT scans of a 3D-printed EMCC sample; (b) image stacking and reconstruction; and (c) image of the mixed phases (left), grains (middle) and fibers (right).

that the viscosity and shear stress of EMCC6 were greater than those of EMCC3 at the same shear rate (Fig. 1a and b).

The readily prepared printable slurries mixed with glass microfibers were manually loaded into the feed bin of an automatic 3D printing machine built by China Building Materials Academy (CBMA). Fresh material was pumped through a pipe by screw extrusion (5IK60RGN-CF, 60W) and deposited in specified positions, forming a multi-layered structure. An integrated printer control system in the 3D printing machine enables the controls of coordinate (x, y, and z in 450 × 450 × 450 mm^3), moving speed of printing head (0–30 mm/s), and speed of slurries pumping (0–10 mL/s) (Fig. 1**c**). In this work, the printing parameters were set as follows: moving speed of printing head in 20 mm/s, pumping speed of the slurries in 1.57 mL/s, and filament diameter of 10 mm. The parameters were optimized according to our experiences and the results reported in the literature [12,43,44]. The freshly printed EMCC filaments and the finished EMCC units (6 filaments in width for the bottom layer, and 4 filaments for the upper 3 layers) are displayed in Fig. 1**d and e**. It is worth mentioning that the printed specimens did not undergo significant deformation within 24 h. The printed EMCC units were stored in a curing chamber (temperature of 23 ℃ and relative humidity >65%) until the testing age (after one year).

Specimens of different sizes were pre-tested. For demonstration, only representative samples were analyzed. Small cuboids (around 6 mm × 6 mm × 6 mm) including both the matrix and interface between filaments were cut from the central part of each EMCC unit. The size of the samples was selected to keep the resolution of XCT images, as a larger sample for XCT tests generally causes a coarser resolution of the obtained X-ray projections.

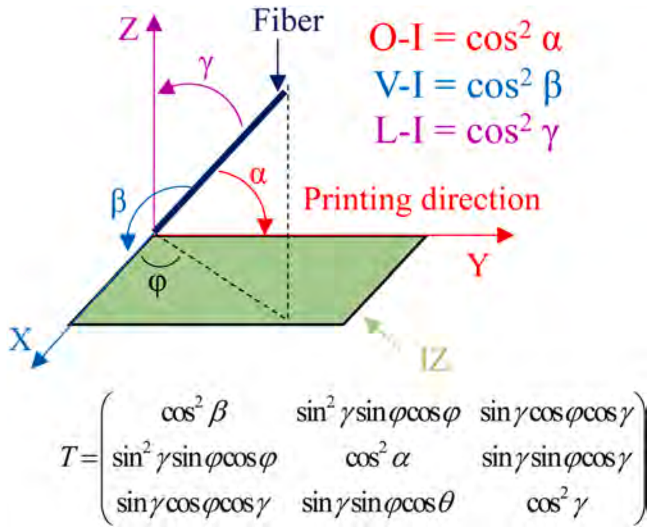

Fig. 3. Directional indexes for fiber distribution (*O-I*, *V-I* and *L-I*) and orientation tensor.

2.3. XCT test and phase analysis

XCT tests were performed in a XTH255/320 LC device (Nikon, Japan). An EMCC sample was first fixed on the sample frame between the X-ray emitter and the detector with the pixels of 2000v× 2000 h (Fig. 2**a**). The X-ray emission parameters were set as 100 kV and 60 μA. A thin Cu film (0.5 mm) was attached on the X-ray emitter to filter the X-ray noises. As X-ray beams penetrate through a material, they attenuate due to the complex interactions between the X-ray and material [45,46], such that projections with different X-ray signal intensities at different spatial positions can non-destructively provide the material information. The exposure time was set as 708 ms, and the complete scans generated 2500 X-ray projections with the resolution of 5 μm/pixel in 30 min.

The massive X-ray projections were subsequently loaded into the CT3dpro software for screening the data quality (Fig. 2**b**). Afterwards, all qualified X-ray projections were stacked for 3D structure computing [47]. Further noise filtering and X-ray attenuation corrections were performed to improve the quality of images.

Successive operations of ROI segmentation, threshold segmentation, filter treatment, fiber extraction, reconstruction and multi-pattern illustration were conducted [27]. Before rigorous 3D structure reconstruction, a region of interest (ROI) for each sample was selected to representatively demonstrate the materials' structure. Here, the ROI of

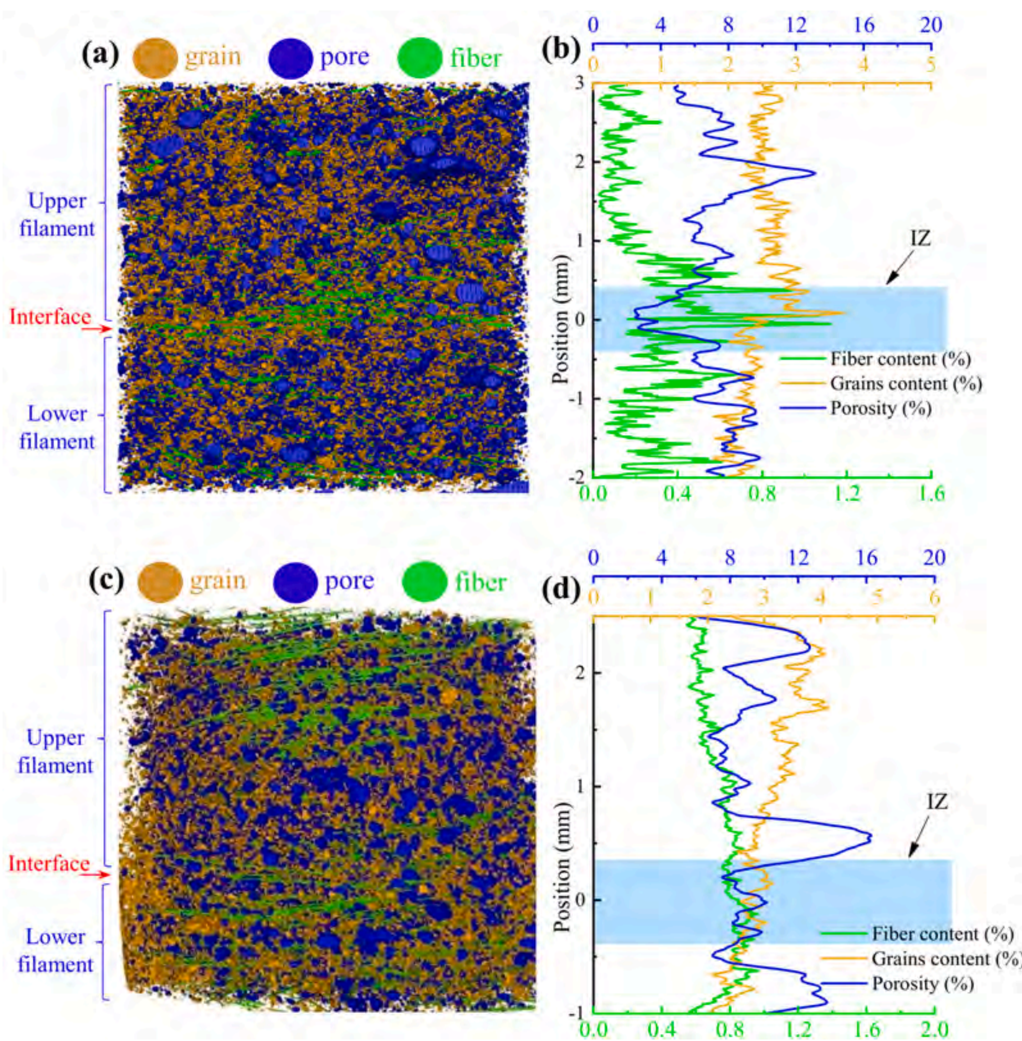

Fig. 4. 3D structure and vertical distributions of fibers, cement grains and pores in EMCC3 (a, b) and EMCC6 (c, d). The interface between the upper and lower filaments was set as 0 in the y-axis of b and d (green = glass microfibers, brown = anhydrous cement grains, blue = pores, transparent areas = the other phases including calcium silicate hydrates (CSH) and other cement hydrates).

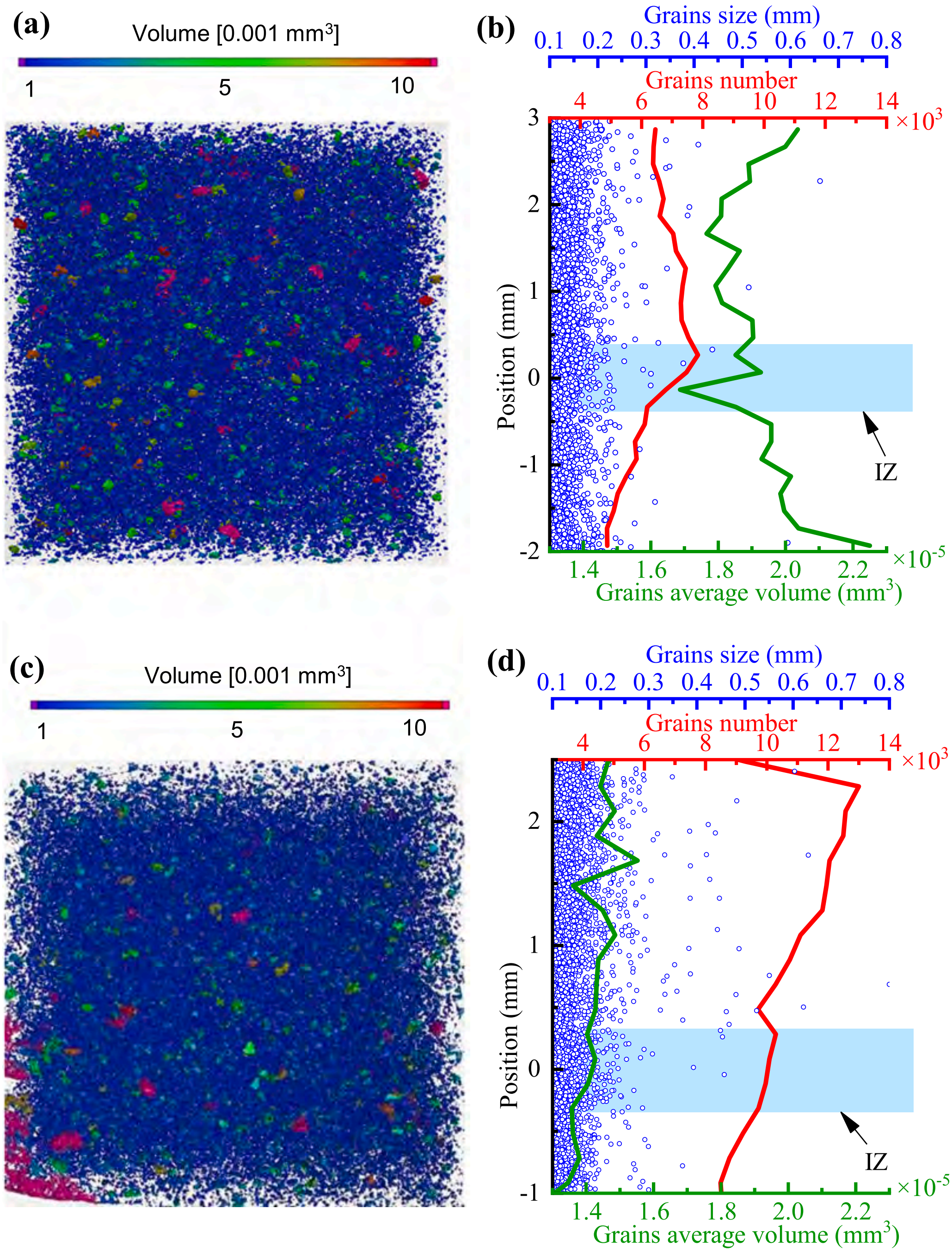

Fig. 5. 3D structure resolved by XCT and distribution (size, volume and number) of cement grains in EMCC3 (a, b) and EMCC6 (c, d).

$5 \times 5 \times 5$ mm^3 containing both the matrix and interlayer for each EMCC sample was elaborately selected (Fig. 2**c**). A geometry-and volume-based segmentation method was applied to resolve the 3D structure and distribution of glass microfibers (see Appendix B for more details of the method).

2.4. Fiber orientation assessment

For the analysis of fiber orientation distribution, traditional measurements assume that each fiber is straight, and ignore the effects of length changes and the fracture of the fibers during extrusion molding [15,16,28]. Those assumptions may be acceptable for rigid and stiff macro fibers (e.g., steel fibers) in EMCC. In this case, the high slenderness of the glass microfibers may be tortured under the shearing actions during extrusion molding. Here, each fiber was divided into the size of the voxel level, and the direction of those divided voxels in the fiber was adopted to measure the fiber orientation. In the material level, the directions of all fiber voxels in ROI were counted to statistically analyze the fiber orientation distribution [27]. When assessing the 3D orientation distributions, the print direction was set as the reference direction. The fiber module and material/pore inclusion module in the VGstudio3.0MAX software were used for fiber, pore and cement grain particle analyses.

To quantify the fiber orientation distribution, directional indexes were used to assess the orientation of fibers. Assume that the O axis is the printing direction (Y axis), the L axis is perpendicular to the interlayer plane (Z axis), and the V axis is perpendicular to the printing direction in the interlayer plane (X axis) (Fig. 3), then three indexes, i.e., the fiber

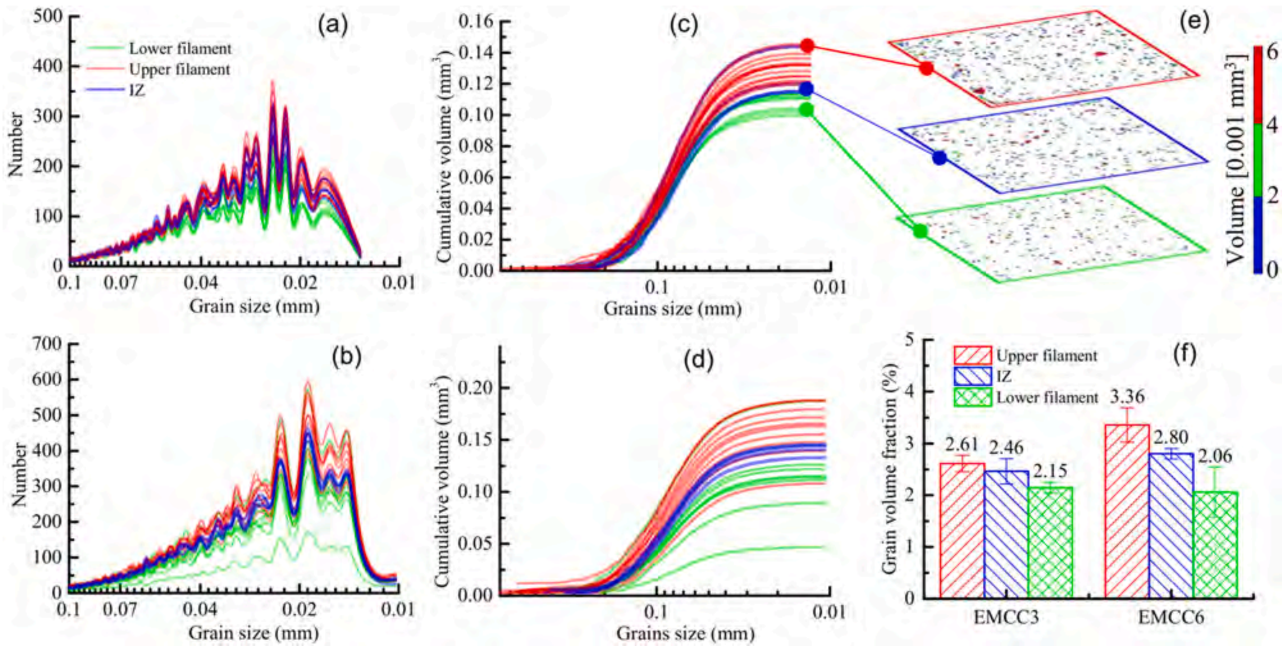

Fig. 6. PND and PSD curves for EMCC3 (a and c) and EMCC6 (b and d); (e) typical XCT images (thickness of 0.2 mm) in the upper filament, lower filament and IZ (the particle size smaller than 0.1 mm were excluded for better illustration); (f) grain volume fractions in the upper filament, IZ and lower filament in EMCC3 and EMCC6.

orientation index ($O\text{-}I = \cos^2\alpha$), stratification index or layer index ($L\text{-}I = \cos^2\gamma$) and vertical index ($V\text{-}I = \cos^2\beta$), can be obtained. The stratification index measures the deviation of a fiber from the direction L. In the case of L-I = 0, the fibers are distributed parallel to the interlayer plane. The vertical index refers to the distribution of a fiber in the horizontal plane perpendicular to the printing direction. Note that the sum of the three coefficients equals to1 ($O\text{-}I + L\text{-}I + V\text{-}L = 1$).

3. Results and discussion

3.1. General outcomes

Fig. 4 selectively and representatively displays 3D images of the EMCC ROIs containing different phases and their distributions perpendicular to the interlayer plane. An interlayer zone (IZ) between two EMCC filaments can be generally identified according to the porosity changes and the thickness of IZ is affected by printing parameters and materials with typical values of 0.2–3 mm [48,49]. In this work, a clear gap between the upper and lower filaments can be observed (Figure B.1). The changes of porosity in IZ are probably owning to the lubrication layer formed in the outer area of filaments during extrusion printing [48]. Considering the porosity variation and the lubrication, the IZ thickness was set as 0.8 mm (Fig. 4 **a and c**).

For the fiber content distribution in EMCC3, a peak of fiber content up to 1.1% was observed, heavily higher than the designed fiber content of 0.3% (Fig. 4**b**). A slight fiber rise (fiber content = 0.96%) was observed near the IZ in EMCC6 (Fig. 4**d**). The uneven distribution of fiber contents indicates the great impacts of extrusion on microstructure of EMCC. The rises of fiber content near the IZ indicated that the fibers gradually migrated to the interface of the filaments (or the inner surface of the pumping pipe) during extrusion printing owing to the uneven shearing forces. Similar observations of fiber accumulation near the filaments' surface were reported for 3D printed polymer composites [41, 42].

For the anhydrous cement grains, the content in the upper filament (3.70% for EMCC3 and 4.12% for EMCC6) was systematically higher than that in the lower filament (2.59% for EMCC3 and 3.04% for EMCC6) (Fig. 4**b and d**). This is caused by the sinking of cement grains in each filament due to the effect of gravity. A peak of the anhydrous cement grain distribution was observed near the IZ in EMCC3 (Fig. 4**b**), evidencing the gather of the anhydrous cement grains. In general, the results of Fig. 4 suggested that both the fibers and anhydrous cement particles may migrate towards the IZ between the upper and lower filaments.

3.2. Analysis of anhydrous cement grains

To understand the transport of cement grains during extrusion molding, specific analysis on thin slice with the thickness of 0.2 mm was performed on the ROIs, and the distributions of grain number, individual size and average size in each slice were output (Fig. 5). For EMCC3, along with the vertical direction from up to down, the average particle size of the cement grains decreased first and then increased, while their number increased first and then decreased. This implied that smaller cement grains were more likely to migrate into the IZ under uneven shearing forces, while larger cement grains stayed in the matrix (Fig. 5**a and b**).

For EMCC6, the trend of grain number and average size showed strong difference (Fig. 5**c and d**). Specifically, they both decreased from up to bottom and no shifts appeared at the IZ. Interestingly, the grain number density was below 8000 (in 5 mm^3) with the average grain volume higher than 1.6×10^{-5} mm^3 in all positions of EMCC3 (Fig. 5**b**). However, the grain number density was over 8000 with the average grain volume lower than 1.6×10^{-5} mm^3 at all positions of EMCC6 (Fig. 5**d**). The thinner grain size and more grain number near the IZ of EMCC3 may be associated to the particle migration under the shearing forces during pumping [17]. During concrete pumping, a water bleeding layer (or lubricate layer) containing more thin particles and water can form on the pumping tube inner surface [43,44,50], which may enhance hydration of the cement grains [51–54]. The accelerated cement hydration, in turn, decreases the size of the anhydrous cement grains.

To further demonstrate the material differences between the IZ and matrix in EMCCs, particle number distribution (PND) and particle size distribution (PSD) were analyzed (Fig. 6). The PND and PSD curves were plotted based on the data in 3–10 slices for EMCC3 (Fig. 6**a and c**) and EMCC6 (Fig. 6**b and d**), and typical layers of 0.2 mm in thickness were

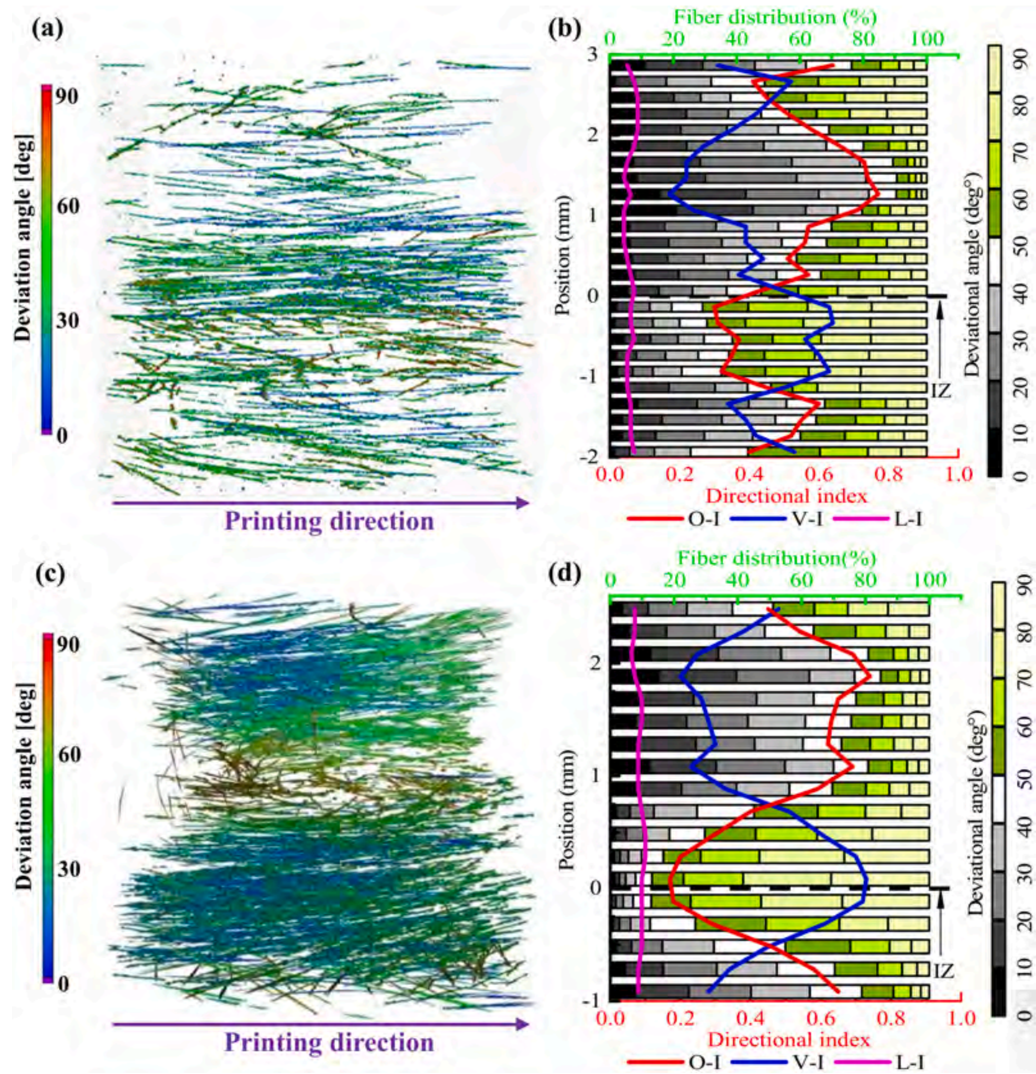

Fig. 7. 3D image resolved by XCT and directional distribution (directional index and deviational angle of printing direction) of fibers in EMCC3 (a, b) and EMCC6 (c, d).

extracted from the upper filament, lower filament and IZ for demonstration (Fig. 6**e**).

Similar PND and PSD trends in the matrix and IZ of the EMCCs were observed. Most of the number was determined by the grains with the size between 0.015 and 0.06 mm (Fig. 6**a and b**), and most of the volume was occupied by the grains with the size between 0.04 and 0.2 mm (Fig. 6**c and d**). The PND and PSD results indicated that the thin particles dominate the number distribution, while the large particles determine the volume distribution for a powder system like cement grains [55,56]. Compared with EMCC6 that showed the concentrated PND in the size range of 0.01–0.02 mm with the PND intensity of 200–700 (Fig. 6**b**), EMCC3 showed the concentrated PND in a bigger size range (0.02–0.03 mm) with a lower PND intensity (100−500) (Fig. 6**a**). When glancing at the PSD curves and typical layers (Fig. 6**e**), the cement grain volume in the upper filament was higher than that in the lower filament due to the sink of the cement grains under the gravity forces, while the cement grain volume in IZ was between them for both EMCC3 (Fig. 6**c**) and EMCC6 (Fig. 6**d**).

Statistic cement grain volume fractions in the IZ, upper filament, and lower filament are illustrated in Fig. 6**f**. Clearly, the cement grain volume fractions of the IZ and upper filament of EMCC6 were 2.802% and 3.358%, higher than those of EMCC3 (2.462% and 2.613%) by 13.81% and 28.51%, respectively. Similar cement grain volume fractions between EMCC3 (2.146%) and EMCC6 (2.060%) were observed in the lower filament (Fig. 6**f**). The grain volume fraction of the lower filament in EMCC3 was less than that of the upper filament by 17.9%, while by 38.7% in EMCC6. The results indicated that increasing fiber content would enhance the difference of cement grain volume fraction among the IZ, upper filament, and lower filament (Fig. 6**f**). This was probably owing to the fact that the higher flowability is required for the cementitious slurries with more microfibers, so cement grains are more likely to sink under the gravity actions [57,58]. Therefore, in each filament, the bottom part of the upper filament always contains more cement grains than the top part of the lower filament in our case (Fig. 6).

3.3. Analysis of glass microfibers

Fig. 7 demonstrates 3D images of the glass microfibers and their directional distributions. It can be seen that fibers generally present an obvious stratification distribution along with the printing direction (Fig. 7**a and c**). Specific analysis on thin layers with the thickness of 0.2 mm was performed. For both EMCC3 and EMCC6, the stratification coefficient (or layer index) (LI) is basically close to 0 (Fig. 7**b and d**), confirming that fibers follow the stratification distribution ($\cos^2\alpha \approx 0.1$; see Fig. 3). In other words, the glass microfibers, at any position of the specimens, are distributed parallel to the IZ, which may be caused by the

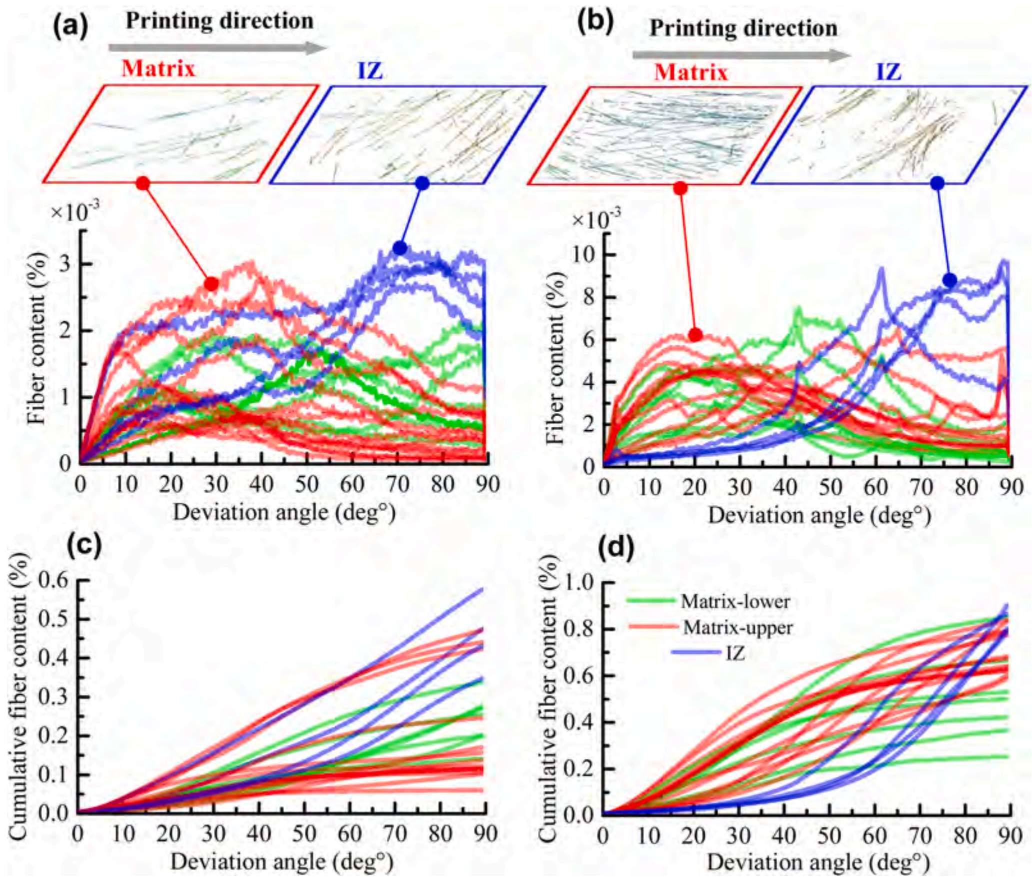

Fig. 8. Selective demonstrations and fiber directional distributions in the upper filament, lower filament and IZ in EMCC3 (a, c) and EMCC6 (b, d).

uneven shearing forces parallel to the IZ plane [42]. The stratified microfibers, in turn, would impact the distribution of shearing forces, consequently, the microfibers, like micro cement grains, may migrate to the IZ.

As *L-I* was closed to 0.1, *O-I* and *V-I* basically played the complementary roles on the determination of fiber directional distribution (*L-I*+*O-I*+*V-I*=1, Fig. 3). Here, only the results of *O-I* and the corresponding angle (α) were taken as the examples to demonstrate the results. The angle of the fibers deviating from the printing direction (α) was also plotted in Fig. 7**b and d**. From the histogram of deviational angle with position, it can be easily found that the fibers in the matrix of filaments mainly distributed within 50°, evidencing the strongly orientated distribution of the glass microfibers in EMCC3 and EMCC6 (Fig. 7**b and d**). However, the fibers in or close to the IZ between two filaments mainly possessed the deviational angles over 50°, suggesting that those fibers were not following the printing direction. The fiber orientation in IZ changed more severely for the EMCC with higher fiber content. The distribution of *O-I* showed the similar trend with that of α. High *O-I* values up to 0.77 for EMCC3 and 0.74 for EMCC6 were found in the filaments' matrices, indicating that most fibers were aligned following the printing direction. The printing-direction orientated fibers have been widely documented in 3D printed concrete with steel fibers [27,28,59]. In the IZ between two extrusion molded filaments, sharp decreases in *O-I* values down to 0.3 for EMCC3 and to 0.17 for EMCC6 were observed (Fig. 7**b and d**), which again means that the fibers were more likely to be perpendicular to the printing direction. The reasons are due to the change of shearing force for different viscosity, see Section 3.4 for further discussion.

Fiber direction and content distributions were analyzed statistically (Fig. 8). Little differences in direction and content distributions between the upper and lower filaments were probed, while differences rose greatly between the filaments' matrix and IZ. A high proportion of the fibers in IZ emerged at high deviational angles between 50° and 90°, but the fibers in the matrices of filaments appeared at low deviational angles between 10° and 40° (Fig. 8**a and b**). So, fiber content in the matrices of filaments rose rapidly at the low deviational angles, while that in the IZ cumulated greatly at the high deviational angles (Fig. 8**c and d**). The distribution of fibers in this work was consistent with the literature [41,60].

Selective slices of XCT images in the IZ and matrix of filaments are also demonstrated in Fig. 8. Evidently, fibers in the filament matrix of EMCC3, that mainly followed the printing direction, were less than those in the IZ that were roughly perpendicular to the printing direction (Fig. 8**a**). For EMCC6, similar trends of different directional distributions between the fibers in the matrix and those in the IZ were observed (Fig. 8**b**). Interesting, some fibers in the IZ of EMCC3 and EMCC6 were *bent and tortured* (Fig. 8**a and b**), suggesting the occurrence of non-uniform shearing forces on the fibers during extrusion molding. Fibers also agglomerated together in the IZ to form fiber bundles (Fig. 8**b**).

Some characteristic parameters that feature the orientation and content distributions are demonstrated in Fig. 9. Results of the deviation angle at the highest fiber content suggested that fibers in the IZ possessed systematically higher deviation angles (78.4° and 78.1°) than those in the matrices of filaments (41.9°and 37.2°) of EMCC3 and EMCC6 (Fig. 9**a**). Analysis of the value of C_{50} (a value of the deviational angle when the cumulative fraction of glass microfibers is 50% [41,60]) also displayed that the matrices of filaments had much higher fiber content along the printing direction (40.0° and 38.3°) than the IZ (60.1° and 68.9°) (Fig. 9**b**). The *O-I* values of the fibers decreased from 0.55 and 0.58 in the matrices of filaments for EMCC3 and EMCC6, to 0.35 and 0.21 in the IZ with the decrease extents of 36.4% and 63.8%, respectively (Fig. 9**c**). Those results, again, evidenced that the direction of the

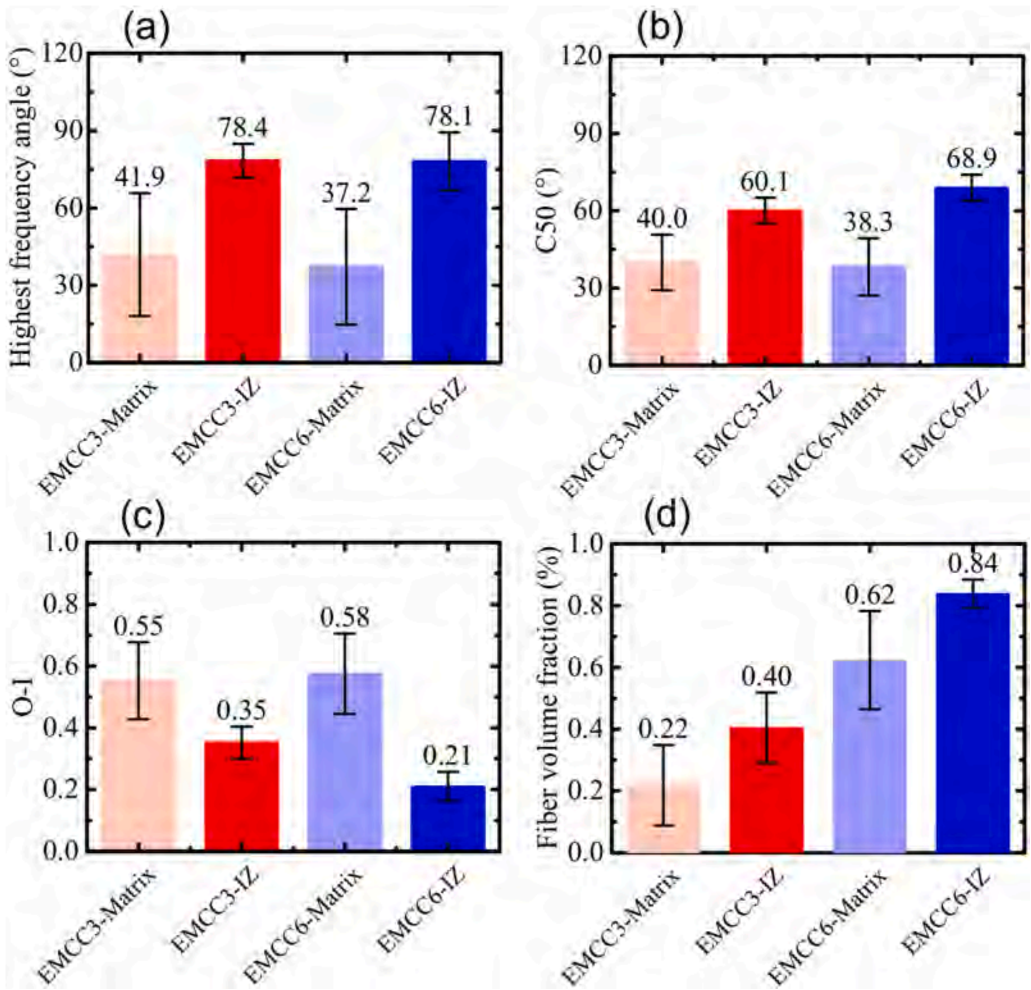

Fig. 9. Results of (a) highest frequency angle, (b) the value of the deviational angle when the cumulative fraction of glass microfibers is 50% (C_{50}), (c) orientation index (O-I) and (d) fiber volume fraction in the matrices and IZ for EMCC3 and EMCC6.

microfibers near the printing tube inner surface was changed during extrusion molding, and this orientation change was severer with the increase of fiber content.

Moreover, different total fiber contents between the matrices of filaments and IZ were obtained. In EMCC3, the total fiber content in IZ was 0.4%, higher than the designed total fiber content (0.3%) by 33.3% and that in the matrices of filaments (0.22%) by 81.8% (Fig. 9**d**). Those data indicated that microfibers may migrate from the matrix to the IZ during extrusion molding. The differences in orientation and content between fibers in the IZ and those in the matrix of extrusion molded filaments were reported for fiber reinforced polymers after 3D printing [41,42], the observations, however, to the best knowledge of the authors, have never been documented for 3D printing cementitious materials elsewhere.

3.4. Discussion on the mechanisms

In this work, the distribution information (including content and direction) of micro cement grains and glass microfibers in EMCCs were resolved with μ-XCT. Non-uniform distribution of the cement grains in filaments was reported. Coarse cement grains were detected to be in the center of the filaments while small grains were more likely to gather in the IZ between the filaments (Figs. 4 and 5). The distribution of those anhydrous cement grains, like the macro particles in concrete during pumping or 3D printing [19,23], would also be affected by the uneven shearing forces during the process of extrusion molding. When particles flow in a thin pipe during pumping, shearing force gradients build up between the central and surface slurries in the pumping pipe. Under the actions of shearing force gradients, grains begin to roll and move along the printing direction. Coarse grains would suffer large shearing force gradients, so they tend to migrate from the surface to the center of the printing pipe (Fig. 10**a**). Additionally, the high shearing forces built near the inner surface of pumping pipe would shrink grains and enhance water bleeding, and this thin bleeding surface layer may also act as the lubricant that improve the slurries' flowability [43,48,50]. Those mechanisms that account for the particle flows during concrete pumping [23] may also work for the transport of grains in EMCC during 3D printing observed in our experiments and those reported in Ref. [19]. The locally raised water content and lowered cement grain size in the IZ between filaments can enhance the hydration of the cement grains [51–54], which may, in turn, further decrease the size of the cement grains in the IZ. Therefore, different distributions of the anhydrous cement grains between the IZ and matrices of EMCC filaments were observed (Figs. 4–6**)**.

In our experimental results, differences in grain content were observed between the upper and lower filaments. Specifically, the top part of the lower filament showed less cement grain content than the bottom part of the upper filament (Fig. 6**f**). This would be the direct consequence of particle sinking in the cementitious slurries due to the gravity actions, similar observations were reported elsewhere [57,58].

The μ-XCT analysis also demonstrated the gathering of glass microfibers in the IZ between two neighbored EMCC filaments (Fig. 9). Such

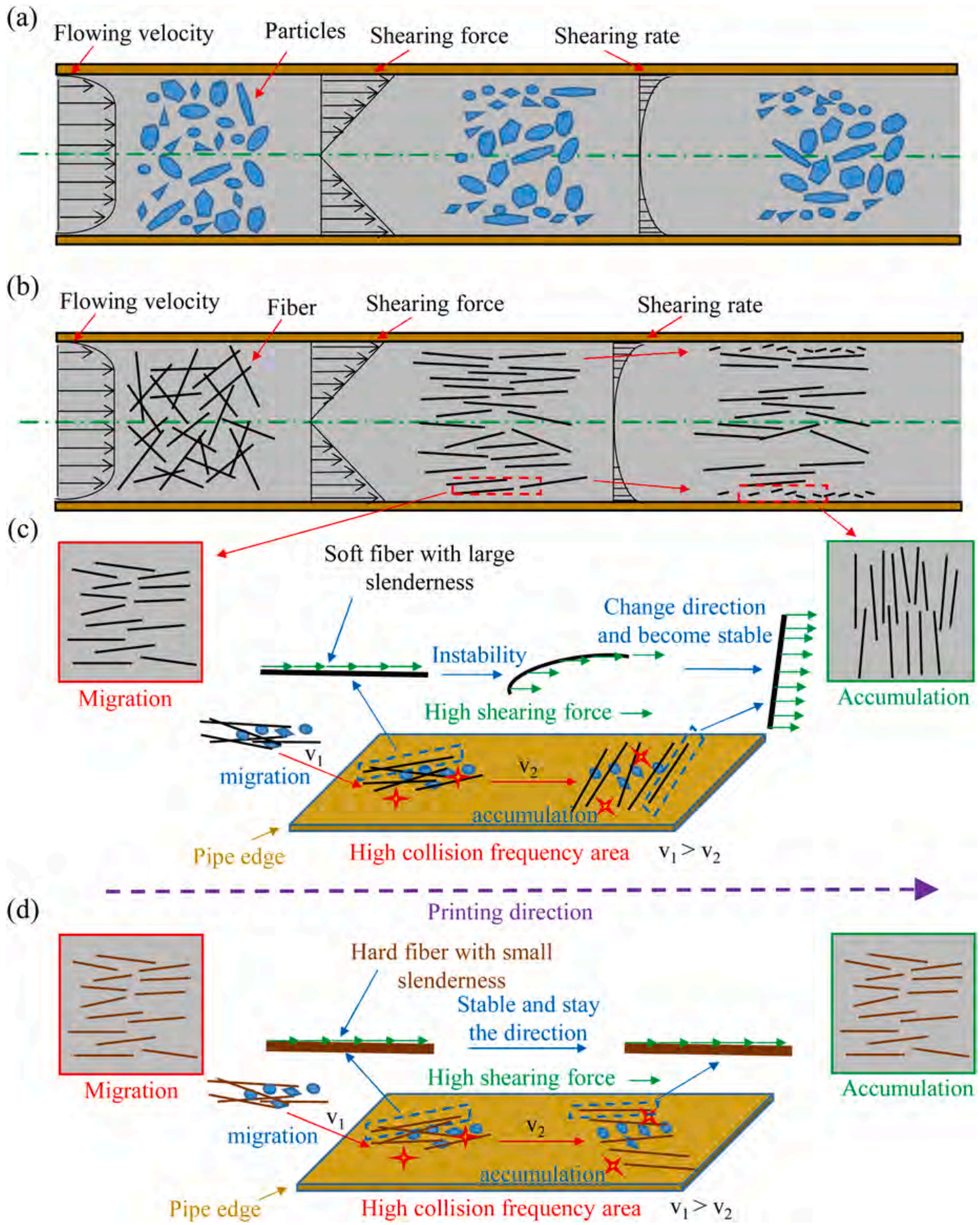

Fig. 10. Schematic diagram of the effect of non-uniform shearing on the distributions of particles (a) and fibers (b); schematic diagram of the effect of high shearing force, collision and fiber stiffness on fiber directional change in interlayer zone for soft fibers (c) and normally rigid fibers (d).

fiber gathering in the surface area was observed for the 3D printed polymer composites with fibers [41,42]. Auernhammer et al. [24] also reported the gathering of tiny glass balls in transparent model concrete. In this case, glass microfibers agglomerated together to form fiber bundles for EMCC6 (Fig. 8**b**). The growth of fiber bundles may course the obstruction of the printing pipe. This is why fiber content lower than 1% was recommended in Refs [16,28] to avoid the blockage of nozzle for EMCC printing.

Orientation analysis of the glass microfibers in EMCCs indicated that most of the glass microfibers followed the printing direction ($L\text{-}I \approx 0.1$ as demonstrated in Fig. 7**b and d**), consistent with the results documented in the literature [27,42]. During extrusion molding, the glass microfibers that were randomly mixed in the slurries suffered uneven shearing actions at different flowing rate. For example, if the two ends of a fiber were at different distances from the surface of the printing pipe, then different shearing stresses and moving speeds rose at the fiber's two

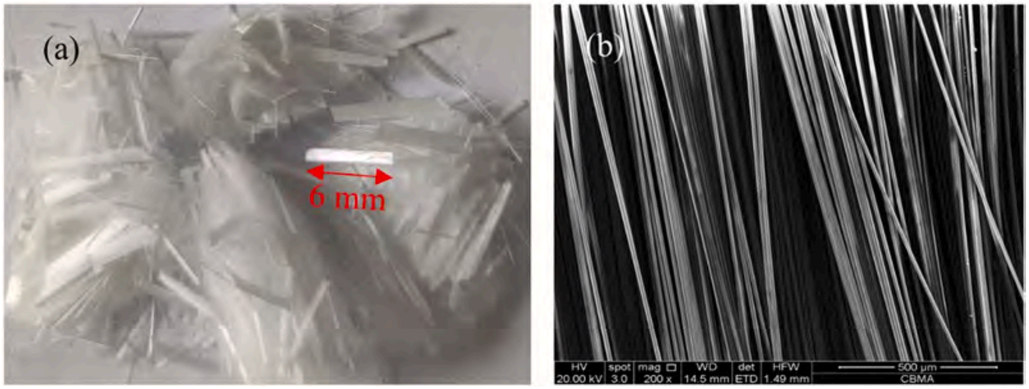

Fig. A.1. (a) Typical photo of the glass microfibers and (b) SEM image.

ends. So the fiber would rotate to diminish the shearing stress gradients, in this way, most glass microfibers were following the printing direction (Fig. 10**b**). The mechanisms also account for the orientation of steel fibers after 3D printing documented elsewhere [26,61].

In this work, however, glass microfibers showed different orientations in the IZ from those in the matrix of filaments ($O\text{-}I = 0.35$ for EMCC3 and 0.21 for EMCC6; Fig. 9**c**). Specifically, the fibers in the IZ were perpendicular to the printing direction (Fig. 8**a and b**). This phenomenon, to the best of the authors, has not been reported elsewhere for 3D printed cementitious materials, but was occasional documented for 3D printed polymer-based composites [41,42]. This would be the consequences of the combined actions of high shearing forces on the slurries confined in the pumping pipe [19,20], large slenderness of glass microfibers with low stiffness [28], as well as high particle collision on the surface of the pumping pipe [17,62]. As illustrated in Fig. 10**c**, to balance the shearing forces, the fibers either follow or are perpendicular to the printing direction [47,63]. For the glass microfibers with high slenderness and low stiffness, the shearing forces would also bend the fibers (Fig. 8**a and b**). The high frequency of particle collisions [17,62] may cause the agglomeration of microfibers to form fiber bundles (Fig. 8**b**). In this work, it indicates that the IZ with fibers perpendicular to the printing direction possessed lower porosity, while the matrix with fibers parallel to the printing direction had higher porosity (Fig. 4). Those would have complex impacts on the mechanical properties of EMCC [48].

It is noteworthy that the premise of forming perpendicularly orientated fibers in IZ is that the fibers should possess thin diameter, large slenderness and low stiffness. Therefore, steel fibers with relatively low slenderness, high stiffness and large diameter [28] are not likely to be bent and agglomerate in the IZ (Fig. 10**d**). It is therefore reasonable that almost all tests on 3D printed steel fiber concrete reported that the fibers follow the printing direction [27,28].

While the distribution characteristics resolved by μ-XCT evidenced the changes in direction and content of cement grains and microfibers between the IZ and matrix of EMCC filaments, some issues still haven't been fully addressed in this present work. First, the resolution of the XCT used is limited (around 5 μm/pixel), therefore a certain portion of the anhydrous cement grains cannot be resolved. This would cause incomplete analysis of the anhydrous cement grains in EMCC. For example, the XCT data in this work did not directly support the hypothesis that the surface bleeding can enhance cement hydration in the IZ between filaments. Second, in this work, the influential factors (such as, printing speed and fiber size) on the distribution of cement grains and microfibers were not tested. While the printing speed was set as 20 mm/s according to the data reported in the literature [12,43,44], the changes in printing speed may change the shearing stresses on the fibers and consequently alter their direction and distribution. More rigorous investigations are wanted to fully address the problems in flows of particles (including both cement grains and fibers) and the impacts of printing patterns towards better controls in materials' structure and properties in 3D printed construction.

Overall, in this work, the changes in direction and content distributions of cement grains and glass microfibers between the IZ and matrix of filaments in EMCCs were reported for the first time. The findings would deepen the understandings in particle flows of EMCCs during 3D printing as well as the designs and controls of 3D printing construction materials.

4. Conclusion

This paper attempted to characterize the distribution of anhydrous cement grains and glass microfiber in EMCC by XCT. Conclusions were drawn as follows:

1. The anhydrous cement grains in EMCC showed a non-uniform distribution between matrix and IZ for uneven shearing force. The smaller particles tended to appear in the IZ while the larger particles were likely to gather in the matrix.
2. Gradient of micro cement grain content rose from the upper filament to the lower filaments. The grain volume fraction of the lower filament in EMCC3 was less than that of the upper filament by 17.9%, while by 38.7% in EMCC6.
3. Glass microfibers gathered in the IZ, with the maximum fiber content up to 1.10% for EMCC3 and 0.96% for EMCC6.
4. Glass microfibers in the matrix of filaments were mostly parallel to the printing direction and these in the IZ were perpendicular to the printing direction in the stratified plane. The orientation index in the matrix of filaments was 0.55 for EMCC3 and 0.58 for EMCC6, while that in the IZ was 0.35 for EMCC3 and 0.21 for EMCC6.
5. The featured distribution of glass microfibers in EMCCs was rooted to the uneven shearing forces during printing. A conceptual model was proposed to capture the mechanisms of change in fibers orientation in the IZ with high shearing stress, low flowing rate and high collision frequency. This model would specifically capture the orientation and distribution of fibers with large slenderness and low stiffness.

Moreover, the results also revealed the mechanism of migration of micro particles/fibers in cementitious slurries under uneven shearing forces during extrusion. The findings will deepen the understandings of particle flow in non-Newtonian liquid and shed much light on tuning and fabricating cementitious composites for digital construction.

CRediT authorship contribution statement

Rijiao Yang: Conceptualization, Methodology, Software, Data curation, Investigation, Writing – original draft. **Yi Zhu:** Methodology, Software. **Yan Lan:** Methodology, Software. **Qiang Zeng:**

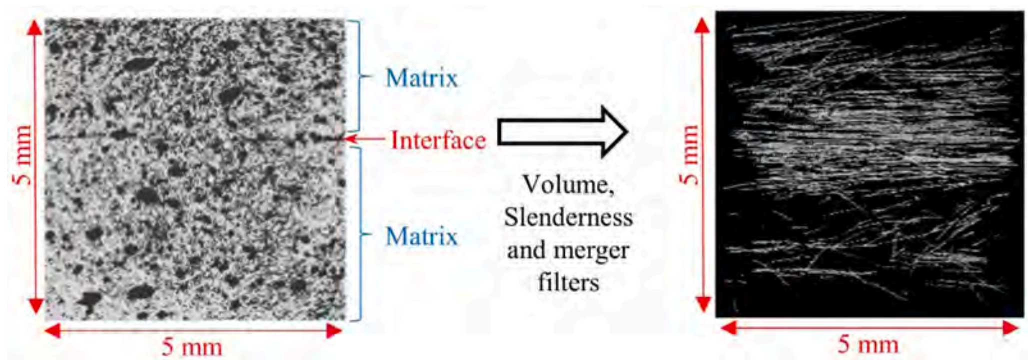

Fig. B.1. Coarse image of a ROI (left) and the resolved fibers after the treatments (right).

Conceptualization, Supervision, Funding acquisition, Methodology, Writing – review & editing. **Yu Peng:** Methodology, Software. **Zhendi Wang:** Conceptualization, Supervision, Funding acquisition, Writing – review & editing.

Declaration of Competing Interest

The authors declare that they have no known competing financial interests or personal relationships that could have appeared to influence the work reported in this paper.

Data availability

Data will be made available on request.

Acknowledgments

This work was supported by the Program Fund of Non-Metallic Excellence and Innovation Center for Building Materials (2022SFP1-1), NSFC (No. 52038004 and 51878602), and the Fundamental Research Funds for the Central Universities, CHD (No. 300102311501).

Appendix A

Glass fibers

Glass fibers with the length of 6 mm and diameter of 20 μm (Fig. A.1) were used to reinforce the cementitious slurries.

Appendix B

Fiber diagnosis and analysis

Due to the little difference of density between glass microfibers (density = 2.70 g/mL) and cement matrix (density =2.58 g/mL), they would show similar gray values in XCT images [64]. Therefore, it is not feasible to directly extract the glass microfibers from the cement matrix by the ordinary gray value thresholding method [27,65]. In this work, enhanced treatments to the XCT images were developed for the extraction of microfibers. First, a filter of volume was used for preliminary segmentation to remove the micro cement grains because their volumes are systematically lower than those of the glass microfibers (V= 0.002 mm^3). However, this filter may fail to filter out all cement grains, because some cement grains can agglomerate together to form a large "cement gain". Therefore, a filter of geometry was employed to remove the agglomerated cement grains, since the slenderness of the glass microfibers is greatly larger than those of the cement grains with and without agglomerations. Later, a smooth treatment was performed to eliminate the cement grain particles attached to or close to the glass microfibers. Those treatments allow us to clearly distinguish between the glass microfibers and the cement matrix (Fig. B.1), while they possess the similar density. Here, 25 slices in EMCC6 were tested to validate the proposed treatments. The results showed the fiber contents between 0.4% and 0.9%, with the average value of 0.66%, close to the design fiber content (0.6%). This suggested that our treatments are reliable to extract the fibers for the cement matrix with similar density. After the preliminary enhanced imaging treatments, all three main phases, i.e., glass microfibers, cement grains and pores, were readily constructed for further analyses.

References

[1] P. Shakor, S. Nejadi, S. Sutjipto, G. Paul, N. Gowripalan, Effects of deposition velocity in the presence/absence of E6-glass fibre on extrusion-based 3D printed mortar, Addit. Manuf. 32 (2020), 101069, https://doi.org/10.1016/j.addma.2020.101069.
[2] J. Xiao, H. Liu, T. Ding, Finite element analysis on the anisotropic behavior of 3D printed concrete under compression and flexure, Addit. Manuf. 39 (2021), 101712, https://doi.org/10.1016/j.addma.2020.101712.
[3] T. Ooms, G. Vantyghem, R. Van Coile, W. De Corte, A parametric modelling strategy for the numerical simulation of 3D concrete printing with complex geometries, Addit. Manuf. 38 (2021), 101743, https://doi.org/10.1016/j.addma.2020.101743.
[4] A. du Plessis, A.J. Babafemi, S.C. Paul, B. Panda, J.P. Tran, C. Broeckhoven, Biomimicry for 3D concrete printing: a review and perspective, Addit. Manuf. 38 (2021), 101823, https://doi.org/10.1016/j.addma.2020.101823.
[5] C. Vlachakis, M. Perry, L. Biondi, J. McAlorum, 3D printed temperature-sensing repairs for concrete structures, Addit. Manuf. 34 (2020), 101238, https://doi.org/10.1016/j.addma.2020.101238.
[6] L. Wang, Y. Liu, Y. Yang, Y. Li, M. Bai, Bonding performance of 3D printing concrete with self-locking interfaces exposed to compression–shear and compression–splitting stresses, Addit. Manuf. 42 (2021), 101992, https://doi.org/10.1016/j.addma.2021.101992.
[7] X. Sun, J. Zhou, Q. Wang, J. Shi, H. Wang, PVA fibre reinforced high-strength cementitious composite for 3D printing: Mechanical properties and durability, Addit. Manuf. 49 (2022), 102500, https://doi.org/10.1016/j.addma.2021.102500.
[8] Y. Zhang, Y. Zhang, W. She, L. Yang, G. Liu, Y. Yang, Rheological and harden properties of the high-thixotropy 3D printing concrete, Constr. Build. Mater. 201 (2019) 278–285, https://doi.org/10.1016/j.conbuildmat.2018.12.061.
[9] A.V. Rahul, M. Santhanam, H. Meena, Z. Ghani, 3D printable concrete: mixture design and test methods, Cem. Concr. Compos. 97 (2019) 13–23, https://doi.org/10.1016/j.cemconcomp.2018.12.014.
[10] S.A.O. Nair, G. Sant, N. Neithalath, Mathematical morphology-based point cloud analysis techniques for geometry assessment of 3D printed concrete elements, Addit. Manuf. 49 (2022), 102499, https://doi.org/10.1016/j.addma.2021.102499.
[11] X. Liu, B. Sun, The influence of interface on the structural stability in 3D concrete printing processes, Addit. Manuf. 48 (2021), 102456, https://doi.org/10.1016/j.addma.2021.102456.
[12] V.N. Nerella, S. Hempel, V. Mechtcherine, Effects of layer-interface properties on mechanical performance of concrete elements produced by extrusion-based 3D-printing, Constr. Build. Mater. 205 (2019) 586–601, https://doi.org/10.1016/j.conbuildmat.2019.01.235.
[13] T.T. Le, S.A. Austin, S. Lim, R.A. Buswell, R. Law, A.G.F. Gibb, T. Thorpe, Hardened properties of high-performance printing concrete, Cem. Concr. Res. 42 (2012) 558–566, https://doi.org/10.1016/j.cemconres.2011.12.003.
[14] B. Panda, S.C. Paul, M.J. Tan, Anisotropic mechanical performance of 3D printed fiber reinforced sustainable construction material, Mater. Lett. 209 (2017) 146–149, https://doi.org/10.1016/j.matlet.2017.07.123.
[15] A.R. Arunothayan, B. Nematollahi, R. Ranade, S.H. Bong, J.G. Sanjayan, K. H. Khayat, Fiber orientation effects on ultra-high performance concrete formed by 3D printing, Cem. Concr. Res. 143 (2021), 106384, https://doi.org/10.1016/j.cemconres.2021.106384.

[16] J. Zhou, J. Lai, L. Du, K. Wu, S. Dong, Effect of directionally distributed steel fiber on static and dynamic properties of 3D printed cementitious composite, Constr. Build. Mater. 318 (2022), 125945, https://doi.org/10.1016/j.conbuildmat.2021.125948.
[17] X. Xie, L. Zhang, C. Shi, X. Liu, Prediction of lubrication layer properties of pumped concrete based on flow induced particle migration, Constr. Build. Mater. 322 (2022), 126115, https://doi.org/10.1016/j.conbuildmat.2021.126115.
[18] B. Lu, Y. Weng, M. Li, Y. Qian, K. Fai Leong, M. Jen Tan, S. Qian, A systematical review of 3D printable cementitious materials, Constr. Build. Mater. 207 (2019) 477–490, https://doi.org/10.1016/j.conbuildmat.2019.02.144.
[19] E. Secrieru, W. Mohamed, S. Fataei, V. Mechtcherine, Assessment and prediction of concrete flow and pumping pressure in pipeline, Cem. Concr. Compos. 107 (2020), 103495, https://doi.org/10.1016/j.cemconcomp.2019.103495.
[20] D. Feys, How much is bulk concrete sheared during pumping, Constr. Build. Mater. 223 (2019) 341–351, https://doi.org/10.1016/j.conbuildmat.2019.06.224.
[21] M. Chen, L. Yang, Y. Zheng, L. Li, S. Wang, Y. Huang, P. Zhao, L. Lu, X. Cheng, Rheological behaviors and structure build-up of 3D printed polypropylene and polyvinyl alcohol fiber-reinforced calcium sulphoaluminate cement composites, J. Mater. Res. Technol. 10 (2021) 1402–1414, https://doi.org/10.1016/j.jmrt.2020.12.115.
[22] Z. Zhao, M. Chen, J. Xu, L. Li, Y. Huang, L. Yang, P. Zhao, L. Lu, Mix design and rheological properties of magnesium potassium phosphate cement composites based on the 3D printing extrusion system, Constr. Build. Mater. 284 (2021), 122797, https://doi.org/10.1016/j.conbuildmat.2021.122797.
[23] S. Fataei, E. Secrieru, V. Mechtcherine, N. Roussel, A first-order physical model for the prediction of shear-induced particle migration and lubricating layer formation during concrete pumping, Cem. Concr. Res. 147 (2021), 106530, https://doi.org/10.1016/j.cemconres.2021.106530.
[24] G.K. Auernhammer, S. Fataei, M.A. Hausteind, H.P. Patela, R. Schwarze, E. Secrieru, V. Mechtcherine, Transparent model concrete with tunable rheology for investigating flow and particle-migration during transport in pipes, Mater. Des. 193 (2020), 108673, https://doi.org/10.1016/j.matdes.2020.108673.
[25] Q. Jiang, Q. Liu, S. Wu, H. Zheng, W. Sun, Modification effect of nanosilica and polypropylene fiber for extrusion-based 3D printing concrete: printability and mechanical anisotropy, Addit. Manuf. 56 (2022), 102944, https://doi.org/10.1016/j.addma.2022.102944.
[26] H. Huang, X. Gao, L. Teng, Fiber alignment and its effect on mechanical properties of UHPC: an overview, Constr. Build. Mater. 296 (2021), 123741, https://doi.org/10.1016/j.conbuildmat.2021.123741.
[27] L. Pham, P. Tran, J. Sanjayan, Steel fibres reinforced 3D printed concrete: influence of fibre sizes on mechanical performance, Constr. Build. Mater. 250 (2020), 118785, https://doi.org/10.1016/j.conbuildmat.2020.118785.
[28] M. Hambach, M. Rutzen, D. Volkmer, Properties of 3D-printed fiber-reinforced portland cement paste, 3D Concr. Print. Technol. (2019) 73–113, https://doi.org/10.1016/B978-0-12-815481-6.00005-1.
[29] T. Ding, J. Xiao, S. Zou, J. Yu, Flexural properties of 3D printed fibre-reinforced concrete with recycled sand, Constr. Build. Mater. 288 (2021), 123077, https://doi.org/10.1016/j.conbuildmat.2021.123077.
[30] S.H. Bong, B. Nematollahi, M. Xia, S.H. Ghaffar, J. Pan, J. Dai, Properties of additively manufactured geopolymer incorporating mineral wollastonite microfibers, Constr. Build. Mater. 331 (2022), 127282, https://doi.org/10.1016/j.conbuildmat.2022.127282.
[31] J. Archez, N. Texier-Mandoki, X. Bourbon, J.F. Caron, S. Rossignol, Shaping of geopolymer composites by 3D printing, J. Build. Eng. 34 (2021), 101894, https://doi.org/10.1016/j.jobe.2020.101894.
[32] A. Singh, Q. Liu, J. Xiao, Q. Lyu, Mechanical and macrostructural properties of 3D printed concrete dosed with steel fibers under different loading direction, Constr. Build. Mater. 323 (2022), 126616, https://doi.org/10.1016/j.conbuildmat.2022.126616.
[33] M.A. Vicentea, G. Ruizb, D.C. Gonzáleza, J. Míngueza, M. Tarifac, X. Zhang, Effects of fiber orientation and content on the static and fatigue behavior of SFRC by using CT-Scan technology, Int. J. Fatigue 128 (2019), 105178, https://doi.org/10.1016/j.ijfatigue.2019.06.038.
[34] H. Huang, X. Gao, K.H. Khayat, Contribution of fiber alignment on flexural properties of UHPC and prediction using the Composite Theory, Cem. Concr. Compos. 118 (2021), 103971, https://doi.org/10.1016/j.cemconcomp.2021.103971.
[35] A. Abrishambaf, M. Pimentel, S. Nunes, Influence of fibre orientation on the tensile behaviour of ultra-high performance fibre reinforced cementitious composites, Cem. Concr. Res. 97 (2017) 28–40, https://doi.org/10.1016/j.cemconres.2017.03.007.
[36] S.T. Kang, J.K. Kim, Numerical simulation of the variation of fiber orientation distribution during flow molding of Ultra High Performance Cementitious Composites (UHPCC), Cem. Concr. Compos. 34 (2012) 208–217, https://doi.org/10.1016/j.cemconcomp.2011.09.015.
[37] W. Meng, K.H. Khayat, Improving flexural performance of ultra-high-performance concrete by rheology control of suspending mortar, Compos. Part B: Eng. 117 (2017) 26–34, https://doi.org/10.1016/j.compositesb.2017.02.019.
[38] L. Martinie, N. Roussel, Simple tools for fiber orientation prediction in industrial practice, Cem. Concr. Res. 41 (2011) 993–1000, https://doi.org/10.1016/j.cemconres.2011.05.008.
[39] J. Liu, S. Li, K. Fox, P. Tran, 3D concrete printing of bioinspired Bouligand structure: A study on impact resistance, Addit. Manuf. 50 (2022), 102544, https://doi.org/10.1016/j.addma.2021.102544.
[40] L. Dong, Y. Yang, Z. Liu, Q. Ren, J. Li, Y. Zhang, C. Wu, Microstructure and mechanical behaviour of 3D printed ultra-high performance concrete after elevated temperatures, Addit. Manuf. 58 (2022), 103032, https://doi.org/10.1016/j.addma.2022.103032.
[41] T. Kunishima, Y. Nagai, S. Nagai, T. Kurokawa, G. Bouvard, J. Abry, V. Fridrici, P. Kapsa, Effects of glass fiber properties and polymer molecular mass on the mechanical and tribological properties of a polyamide-66-based composite in contact with carbon steel under grease lubrication, Wear 462–463 (2020), 203500, https://doi.org/10.1016/j.wear.2020.203500.
[42] D. Yang, H. Zhang, J. Wu, E.D. McCarthy, Fibre flow and void formation in 3D printing of short-fibre reinforced thermoplastic composites: an experimental benchmark exercise, Addit. Manuf. 37 (2021), 101686, https://doi.org/10.1016/j.addma.2020.101686.
[43] Z. Geng, W. She, W. Zuo, K. Lyu, H. Pan, Y. Zhang, C. Miao, Layer-interface properties in 3D printed concrete: dual hierarchical structure and micromechanical characterization, Cem. Concr. Res. 138 (2020), 106220, https://doi.org/10.1016/j.cemconres.2020.106220.
[44] J.G. Sanjayan, B. Nematollahi, M. Xia, T. Marchment, Effect of surface moisture on inter-layer strength of 3D printed concrete, Constr. Build. Mater. 172 (2018) 468–475, https://doi.org/10.1016/j.conbuildmat.2018.03.232.
[45] Q. Zeng, P. Yang, Y. Peng, J. Wang, C. Zhou, Tracing mercury entrapment in porous cement paste after mercury intrusion test by X-ray computed tomography and implications for pore structure characterization, Mater. Charact. 151 (2019) 203–215, https://doi.org/10.1016/j.matchar.2019.02.014.
[46] S. Brisard, M. Serdar, P.J.M. Monteiro, Multiscale X-ray tomography of cementitious materials: a review, Cem. Concr. Res. 128 (2020), 105824, https://doi.org/10.1016/j.cemconres.2019.105824.
[47] Y. Peng, G. Zhao, Y. Qi, Q. Zeng, In-situ assessment of the water-penetration resistance of polymer modified cement mortars by μ-XCT, SEM and EDS, Cem. Concr. Compos. 114 (2020), 103821, https://doi.org/10.1016/j.cemconcomp.2020.103821.
[48] R. Yang, Q. Zeng, Y. Peng, H. Wang, Z. Wang, Anomalous matrix and interlayer pore structure of 3D-printed fiber-reinforced cementitious composites, Cem. Concr. Res. 157 (2022), 106829, https://doi.org/10.1016/j.cemconres.2022.106829.
[49] Y. Chen, C.R. Rodriguez, Z. Li, B. Chen, O. Çopuroğlu, E. Schlangen, Effect of different grade levels of calcined clays on fresh and hardened properties of ternary-blended cementitious materials for 3D printing, Cem. Concr. Compos. 114 (2020), 103708, https://doi.org/10.1016/j.cemconcomp.2020.103708.
[50] D. Feys, Interactions Between Rheological Properties and Pumping of Self-compacting Concrete, Ghent University, Gent, 2009. Ph-D dissertation.
[51] H. Mehdizadeh, X. Jia, K.H. Mo, T. Ling, Effect of water-to-cement ratio induced hydration on the accelerated carbonation of cement pastes, Environ. Pollut. 280 (2021), 116914, https://doi.org/10.1016/j.envpol.2021.116914.
[52] D.M. Kirby, J.J. Biernacki, The effect of water-to-cement ratio on the hydration kinetics of tricalcium silicate cements: testing the two-step hydration hypothesis, Cem. Concr. Res. 42 (2012) 1147–1156, https://doi.org/10.1016/j.cemconres.2012.05.009.
[53] V.T. Nguyen, S.Y. Lee, S. Chung, J. Moon, D.J. Kim, Effects of cement particle distribution on the hydration process of cement paste in three-dimensional computer simulation, Constr. Build. Mater. 311 (2021), 125322, https://doi.org/10.1016/j.conbuildmat.2021.125322.
[54] J.W. Bullard, H.M. Jennings, R.A. Livingston, A. Nonat, G.W. Scherer, J.S. Schweitzer, K.L. Scrivener, J.J. Thomas, Mechanisms of cement hydration, Cem. Concr. Res. 41 (2011) 1208–1223, https://doi.org/10.1016/j.cemconres.2010.09.011.
[55] H. Sun, B. Fan, S.A. Memon, Z. Cen, X. Gao, B. Lin, B. Liu, D. Li, F. Xing, X. Zhang, 3D particle size distribution of inter-ground Portland limestone/slag cement from 2D observations: characterization and distribution evaluation, Constr. Build. Mater. 147 (2017) 550–557, https://doi.org/10.1016/j.conbuildmat.2017.04.070.
[56] Y. Wang, Y. Li, Y. Su, X. He, B. Strnadel, Preparation of waste glass powder by different grinding methods and its utilization in cement-based materials, Adv. Powder Technol. 33 (2022), 103690, https://doi.org/10.1016/j.apt.2022.103690.
[57] Y. Peng, R.A. Lauten, K. Reknes, S. Jacobsen, Bleeding and sedimentation of cement paste measured by hydrostatic pressure and Turbiscan, Cem. Concr. Compos. 76 (2017) 25–38, https://doi.org/10.1016/j.cemconcomp.2016.11.013.
[58] Y. Peng, S. Jacobsen, Influence of water/cement ratio, admixtures and filler on sedimentation and bleeding of cement paste, Cem. Concr. Res. 54 (2013) 133–142, https://doi.org/10.1016/j.cemconres.2013.09.003.
[59] V.C. Lia, F.P. Bos, K. Yu, W. McGee, T.Y. Ng, S.C. Figueiredo, K. Nefs, V. Mechtcherine, V.N. Nerella, J. Pan, G.P.A.G. van Zijl, P.J. Kruger, On the emergence of 3D printable Engineered, Strain Hardening Cementitious Composites (ECC/SHCC), Cem. Concr. Res. 132 (2020), 106038, https://doi.org/10.1016/j.cemconres.2020.106038.
[60] T. Kunishima, Y. Nagai, T. Kurokawa, G. Bouvard, J. Abry, V. Fridrici, P. Kapsa, Tribological behavior of glass fiber reinforced-PA66 in contact with carbon steel under high contact pressure, sliding and grease lubricated conditions, Wear 456–457 (2020), 203383, https://doi.org/10.1016/j.wear.2020.203383.
[61] D. Feys, G. De Schutter, S. Fataei, N.S. Martys, V. Mechtcherine, Pumping of concrete: understanding a common placement method with lots of challenges, Cem. Concr. Res. 154 (2022), 106720, https://doi.org/10.1016/j.cemconres.2022.106720.
[62] H.S. Wong, M.K. Head, N.R. Buenfeld, Pore segmentation of cement-based materials from back scattered electron images, Cem. Concr. Res. 36 (2006) 1083–1090, https://doi.org/10.1016/j.cemconres.2005.10.006.
[63] J. Huang, Y. Zhang, Y. Sun, J. Ren, Z. Zhao, J. Zhang, Evaluation of pore size distribution and permeability reduction behavior in pervious concrete, Constr.

Build. Mater. 290 (2021), 123228, https://doi.org/10.1016/j.conbuildmat.2021.123228.
[64] L. Hong, P. Zhang, D. Liu, P. Gao, B. Zhan, Q. Yu, L. Sun, Effective segmentation of short fibers in glass fiber reinforced concrete's X-ray images using deep learning technology, Mater. Des. 210 (2021), 110024, https://doi.org/10.1016/j.matdes.2021.110024.
[65] W. Wang, A. Shen, Z. Lyu, Z. He, K.T.Q. Nguyen, Fresh and rheological characteristics of fiber reinforced concrete—A review, Constr. Build. Mater. 296 (2021), 123734, https://doi.org/10.1016/j.conbuildmat.2021.123734.